Computational Materials Science 188 (2021) 110150

Contents lists available at ScienceDirect

Computational Materials Science

journal homepage: www.elsevier.com/locate/commatsci

On the significance of model design in atomistic calculations of the Peierls stress in Nb

Wu-Rong Jian [a,*], Shuozhi Xu [a], Irene J. Beyerlein [a,b]

[a] Department of Mechanical Engineering, University of California, Santa Barbara, Santa Barbara, California 93106-5070, USA
[b] Materials Department, University of California, Santa Barbara, Santa Barbara, California 93106-5050, USA

ARTICLE INFO

Keywords:
Atomistic models
Peierls stress
Body-centered cubic
Interatomic potential

ABSTRACT

The Peierls stress required for a single dislocation to glide in a perfect crystal is considered one of the most important properties controlling plastic deformation of metals. Values for the Peierls stress computed by atomistic models often differ even for the same dislocation and when using the same material interatomic potential, limiting their value in understanding material behavior. Here, using molecular static simulations, we study the effects of model configuration, model size, and loading mode on the Peierls stress of an edge dislocation on the {112} glide plane in body-centered cubic Nb in the twinning and anti-twinning senses of slip. The analysis includes six model configurations, a model size range spanning over an order of magnitude, and three loading modes, all repeated for two interatomic potentials for Nb. Results show that, in most cases studied, smaller model sizes artificially lead to lower Peierls stresses. The study also reveals a substantial effect of model configuration on whether the Peierls stress converges with size, the minimum size required for convergence, and the magnitude of the Peierls stress. Only one model configuration, the periodic array of dislocation (PAD) model, achieves a strictly converged value for the two interatomic potentials considered here. In addition, PAD model predicts the lowest Peierls stress values among all model configurations, provided that the model size is sufficiently large. We show that with the same interatomic potential, while one model configuration predicts a higher anti-twinning Peierls stress than twinning Peierls stress, another one may predict the opposite asymmetry. Unlike the stress-controlled loading mode, the shear-controlled and displacement-controlled loading modes provide similar results using both potentials. The findings here will be useful for selecting the appropriate model settings in research studies involving Peierls stress calculations via atomistic simulations.

1. Introduction

Dislocation glide is one of the key mechanisms underlying the plastic deformation of metallic crystals [1]. The minimum resolved shear stress required for a single dislocation to glide on its prescribed glide plane in an otherwise perfect crystal is known as the Peierls stress [2,3]. As a property fundamental to a unit mechanism at the atomic scale, the Peierls stress can be challenging to measure experimentally, and hence, it is most often computed. Currently, two classes of numerical approaches have been used for Peierls stress calculations. One class is atomic-scale calculations, such as molecular statics (MS) simulations [4] and *ab initio* density functional theory (DFT) calculations [5]. The second kind of approach uses a continuum formulation, of which common examples include the Peierls-Nabarro model [6] or a phase-field dislocation model [7]. Continuum models are often informed by atomic-scale calculations and as such, their accuracy in Peierls stress calculations has been quantified by comparisons with atomistic calculations [8]. It is often found that even the most sophisticated continuum models tend to overestimate the Peierls stress [9,10].

Between MS and DFT, DFT is the more reliable approach. However, DFT is not as widely used because it is computationally expensive even when the simulation cell for Peierls stress calculations usually contains no more than hundreds of atoms [11]. On the other hand, in MS simulations, oftentimes up to millions of atoms are employed [12]. In view of the small simulation size in DFT calculations, dislocations in most face-centered cubic (FCC) metals are not accessible since their dissociated distances largely exceed the simulation cell dimensions [5]. Exceptions include Al [13–15] and Ni [16], which attain high intrinsic stacking fault energies (SFE) [17]. Because they have a compact core, DFT simulations have been applied to calculate the Peierls stress in body-

* Corresponding author.
E-mail address: wurong@ucsb.edu (W.-R. Jian).

https://doi.org/10.1016/j.commatsci.2020.110150
Received 20 October 2020; Accepted 29 October 2020
Available online 1 December 2020

centered cubic (BCC) metals. To date, the calculations mainly focus on screw dislocations, since they have much higher Peierls stresses and lower mobility than edge dislocations [18,19]. While the size effects on the Peierls stress have been quantified in selected DFT calculations [21–22], it is difficult to conduct a comprehensive analysis on size effects by further enlarging the model size.

While MS may not yield an estimate as accurate as DFT, it can be a useful approach for analyzing differences in Peierls stresses among slip planes and dislocation characters, for instance. With MS simulations, Peierls stresses have been computed widely, especially as more empirical interatomic potentials are being developed and improved for FCC, BCC, hexagonal close-packed (HCP), and diamond cubic crystals [23–26,4,27–31]. However, with the increased number of studies, it has become evident that the Peierls stress calculated by different researchers can differ significantly even when the same interatomic potential is considered for the same dislocation [32]. For example, using the same model configuration and the same Stillinger-Weber potential [33] but different model sizes, Ren et al. [34] and Koizumi et al. [35] reported two very different values for the Peierls stress of the screw dislocation on the shuffle-set glide plane in Si, which are 5.8 GPa and 2 GPa, respectively.

Apart from the interatomic potential, different model designs have been employed in Peierls stress studies. Model design parameters include the model configurations, model size, and loading modes (e.g., stress-controlled versus displacement-controlled). To date, six model configurations have been used for Peierls stress calculations, including the fixed boundary models, periodic array of dislocation (PAD), dipoles, and quadruple. Atomistic studies indicate that some of these modeling design choices affect the Peierls stress calculation. Chaussidon et al [25] compared the Peierls stress of a screw dislocation gliding by the {110}⟨111⟩ family in two BCC Fe model configurations with different boundary conditions (BCs) and revealed the difference can be up to 300 MPa. These few studies hint that the sensitivities to other model designs may be more critical than first thought. In setting up an atomic model, a number of intrinsic and extrinsic parameters need to be chosen, and to date, there is no guidance on the appropriate settings needed to ensure a reliable Peierls stress calculation. As such it can be imperative that the model is designed to provides estimates that are insensitive to model parameter choices and the calculated trends solely reflect the material variables of interest (e.g., crystallographic planes or dislocation character).

Compared with FCC and HCP metals, dislocations in BCC metals possess much higher Peierls stresses and their motion controls the yielding and plastic deformation behavior of these materials [36–38]. Some BCC metals, like Fe and Nb, behave more ductile than others, and thus their dislocation motion attracts more attention [25,39]. In addition, dislocations with the same Burgers vector $(a_0/2)\langle 111\rangle$ (a_0 is the lattice parameter) can glide on various planes, e.g., {110}, {112}, and {123}, along the same ⟨111⟩ direction [40,41]. In particular, there is a twinning/anti-twinning asymmetry in the Peierls stress on the {112} glide planes [42]. For a given glide plane in the same BCC metal, the Peierls stresses of screw dislocation is usually much higher than that of edge dislocation, reflecting the former's low mobility [43–45].

In this work, we calculate the Peierls stress in Nb, using two interatomic potentials in conjunction with different model configurations, model sizes, and loading modes. Nb is important as a relatively ductile structural metal, while also being the least dense among all BCC refractory metals [46]. Herein, we choose the edge dislocation with the Burgers vector $(a_0/2)\langle 111\rangle$. With this focus, we are able to consider six model configurations, a wide range of model sizes spanning over one order of magnitude, both the twinning and anti-twinning directions, and three loading modes. We repeat the calculations using two interatomic potentials, not as a test of these potentials, but to identify any sensitivities of the trends to the type of interatomic potential used. All these modeling choices have been used in the literature for the Peierls stress calculations. To our best knowledge, this is the first time that model designs are compared in a systematic fashion. With this elaborate set of calculations, we can identify which settings are critical and could affect the results on Peierls stresses.

Ideally, given the same interatomic potential and a model of reasonable size, the Peierls stress ought to not depend on these model design choices. We find that in most cases studied, smaller model sizes lead to lower Peierls stresses. Results also show that the model configuration has a substantial effect on whether the Peierls stress converges with size, the minimum size required for convergence, and the magnitude of the Peierls stress. Among all six model configurations considered, the PAD model is the only one that converges with an increasing model size when either interatomic potential is used. Although the focus here lies on Nb, the trends and recommendations made here are anticipated to apply to other edge dislocations with compact cores in other metals, such as other BCC metals and FCC metals with high SFE (e.g., Al and Ni).

2. Methodology

We use the Large-scale Atomic/Molecular Massively Parallel Simulator (LAMMPS) [49] for the atomistic simulations and two embedded-atom-method (EAM) potentials to describe the atomic interactions between Nb atoms. The two main EAM potentials adopted were proposed by Ackland and Thetford [50], and Lin et al [51]. For simplification, in what follows, we refer to these two as Ackland potential and Lin potential, respectively. They are chosen for two reasons. First, with respect to experimental measurements and DFT calculations, they predict similar lattice parameters and elastic constants, as shown in Table 1. Second, they produce opposing differences in their generalized stacking fault energy (GSFE) curves with respect to DFT, with the one from the Ackland potential predicting values greater than and the Lin potential predicting values lower than DFT, as seen in Fig. 1. It should be noted that we calculate the GSFE curve in MS simulation using the same method as that in the DFT calculation [47] against which our results are compared. Specifically, we use an atomistic model containing 24 {112} atomic planes. First, the top 12 layers of atoms are displaced with respect to the bottom 12 atomic layers along the ⟨111⟩ direction. Then following each incremental displacement, the top three and bottom three layers of atoms are fixed, while the remaining layers are allowed to relax along the ⟨112⟩ direction. This relaxation method was utilized widely in the community, e.g., in FCC [52] and BCC [53,54] metals. The atomic model presented here is for the GSFE curve calculation only. Completely different models and boundary conditions will be used for the Peierls stress calculations.

The GSFE curve based on Ackland potential exhibits a shallow local minimum, which does not exist in the Lin potential- or DFT-derived curve [47]. Prior MS work on a {110}⟨111⟩ edge dislocation in Fe showed that the potential that predicts a local minimum on the GSFE curve produces a split core with a larger spread in the tensile field than the cores produced by other potentials without the local minimum [55]. It was also found that the 0 K Peierls stress of the edge dislocation with the split core is nearly one order of magnitude higher than those based on the other potentials. As will be shown later, a similar phenomenon occurs in our work. To help ensure that conclusions drawn by the

Table 1
Lattice parameter a_0 (in Å), elastic constants C_{11}, C_{12}, C_{44} (in GPa), and unstable stacking fault energy on the {112} plane γ_{usf}^{112} (in mJ/m^2), calculated from the Ackland and Lin interatomic potentials. DFT [47] and experimental (Exp) [48] results are listed as references.

	a_0	C_{11}	C_{12}	C_{44}	γ_{usf}^{112}
Ackland	3.3008	246.85	133.38	28.33	832.09
Lin	3.3	263.56	125.28	35.03	697.23
DFT	3.324	249.01	135.43	18.1	768.82
Exp	3.301	245	132	28.4	

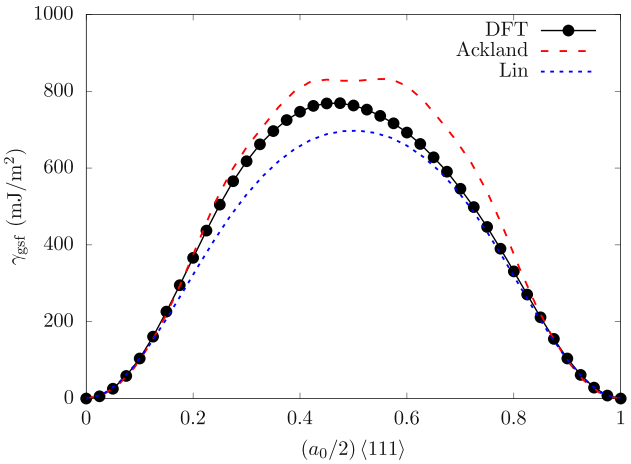

Fig. 1. Relaxed GSFE curves on the {112} plane in Nb, calculated from the Ackland and Lin interatomic potentials. Results based on DFT [47] are presented as references.

present study on model design would apply to a range of potentials, we repeat calculations on these two potentials possessing this significant difference.

We focus these tests of model design on the calculations of the Peierls stress for a $\{112\}\langle 111\rangle$ edge dislocation in Nb. In studies of Peierls stresses in Nb, the {110} plane is often considered [56,18], but recent experimental studies have shown that the {112} plane is also an important glide plane for dislocation slip for Nb, as well as another ductile refractory metal Ta [57–59]. The edge dislocation is chosen, because unlike the screw dislocation [60], it likely remains stable on the glide plane and does not cross slip. In addition, it is computationally much less costly to calculate the Peierls stress of an edge dislocation than a screw dislocation. The savings in computation time allow for a larger range of system sizes for all six model configurations to be examined.

Figure 2 presents six atomistic model configurations that have been used for determining the Peierls stress in the literature to date. They share the same crystallographic orientations, with their dislocation lines lying along the z-axes and the glide plane normal, the y-axis, oriented in the $[11\bar{2}]$ orientation. The other two crystallographic directions are [111] and $[\bar{1}10]$ for the x- and z-axes, respectively. The length of the dislocation line $L_z \approx 1.4$ nm. All the simulations are quasi-3D, meaning that they are 3D crystallographically, but the geometry is such that the problem is effectively 2D.

Based on their BCs, these six model configurations are divided into two groups. The first group contains the three atomistic models with partially periodic boundary conditions, which are the fixed boundary-circle (FBC) [61], fixed boundary-square (FBS) [31] and PAD models [32]. In the FBC and FBS models (Fig. 2(a–b)), the dislocation is inserted via the anisotropic elasticity theory [1] in the center of a cylinder with the diameter of L for the FBC case and a square with a side length of L in the FBS case. Their BCs are partially periodic since periodic BCs are only applied along the dislocation line direction, i.e., the z-axis. Furthermore, each of these two models is divided into the inner and outer regions. The thickness of the outer region (in blue) is larger than the cutoff distance of the potential, which is 5.5 Å for Ackland potential and 7.2 Å for Lin potential. After the dislocation is inserted, atoms in the outer region are fixed, while those in the inner region can relax during the energy minimization. In the PAD model (Fig. 2(c)), the dislocation is constructed by allowing the top half crystal have three more (111) atomic planes than the bottom one, followed by energy minimization. The construction approach is similar to the one used for edge dislocations in Ref. [62,23,4,32]. Hence, unlike the FBC and FBS models, elasticity theory [63] is not used in PAD model. The simulation cell for PAD has the same size as the FBS model, however. The PAD model is partially periodic since the periodic BCs are applied only along both the dislocation slip direction (x-axis) and the dislocation line direction (z-axis), while non-periodic BCs are applied along the y-axis. Atoms in the top and bottom regions in the simulation cell, which have the same thickness as the outer regions in FBC and FBS models, are not allowed to move freely during the energy minimization. However, some details depend on the selected loading mode, which will be described later.

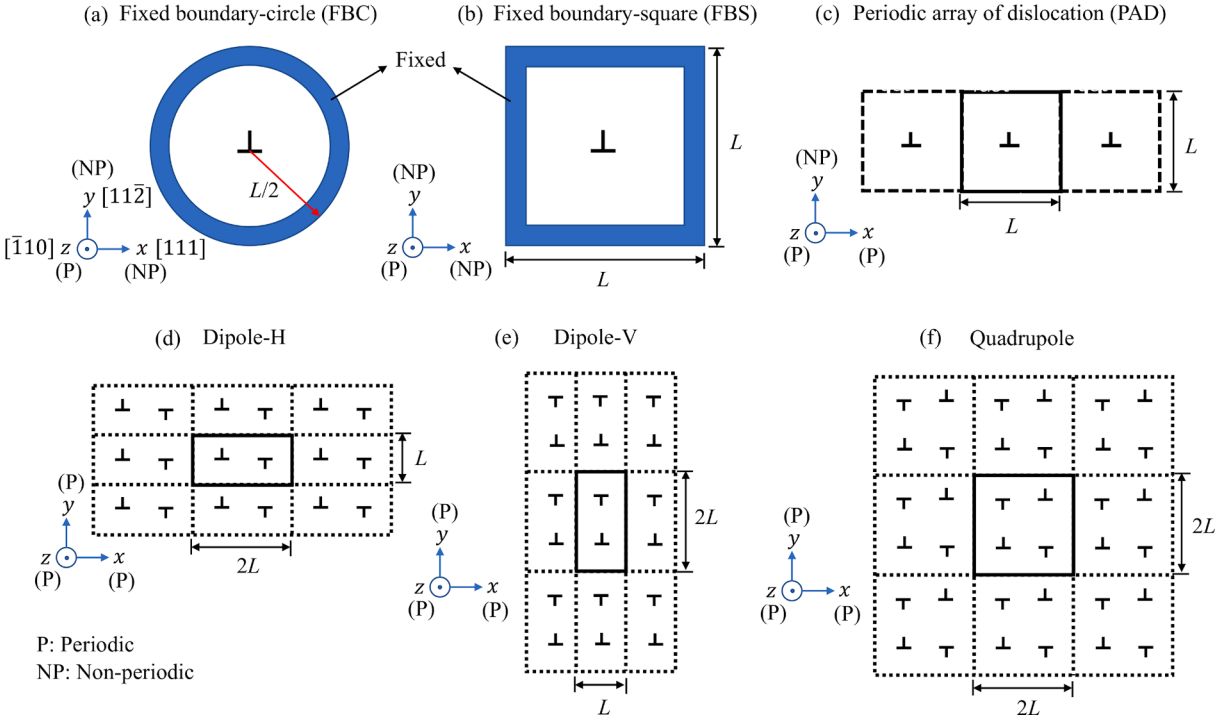

Fig. 2. Schematic of six common model configurations of dislocation: (a) fixed boundary-circle (FBC), (b) fixed boundary-square (FBS), (c) periodic array of dislocation (PAD), (d) horizontal dipole (Dipole-H), (e) vertical dipole (Dipole-V), and (f) quadrupole.

The second group of dislocation models includes the horizontal dipole (dipole-H) [64], vertical dipole (dipole-V) [24], and quadrupole models [65], which use periodic BCs in all three directions (Fig. 2(d–f)). The dislocation is inserted into these models via the same method as used in PAD model, i.e., by introducing three extra half-planes of atoms. Herein, dipole-H and dipole-V models represent the array of two dislocations with the opposite Burgers vectors and placed along the horizontal (x-axis) and vertical (y-axis) directions, respectively. The quadrupole model denotes the array of four dislocations with the alternatively opposite Burgers vectors and placed along both in-plane directions. In the dipole-H model, a minimum L exists below which the dislocation dipole self annihilates during energy minimization prior to loading, which is 15 nm for the Ackland potential and 70 nm for the Lin potential. Thus, values of the Peierls stresses corresponding to L below the critical size will be missing for the dipole-H model. We remark that the annihilation does not occur in any other model within the range of L studied here.

In the FBC and FBS models, anisotropic elasticity theory is used, whereas in the PAD, dipole-H, dipole-V, and quadrupole models, it is not. However, in prior application of the PAD model [66] and dipole-H model [7], isotropic elasticity theory was applied to introduce the dislocations. The difference in the Peierls stress induced by the anisotropic versus isotropic elasticity theory in the PAD and dipole-H models (along with the dipole-V and quadrupole models) should be negligible because the subsequent energy minimization is expected to find the same relaxed dislocation core structures, regardless of the initial structures. The choice of elasticity theory, however, is potentially important in the FBC and FBS models, because the atoms within the outer boundaries are displaced first following the elasticity theory and then fixed during the energy minimization. In other words, because the boundaries are fixed, they are not minimized after inserting the dislocation. To investigate the influences on the Peierls stress, in selected cases, we repeat the calculations in FBC and FBS models using isotropic elasticity theory.

The performance of these six model configurations is assessed by testing their individual size effects on Peierls stress. We vary L over one order of magnitude from 10 nm to 500 nm. The largest size of $L = 500$ nm is beyond that used in usual atomistic simulations. However, utilizing such a wide range of sizes will prove essential for identifying whether convergence in the computed Peierls stress can be obtained, and if so, the required size. The actual value of $L = 500$ nm is merely based on computational limitations and the largest model configuration studied here, the quadrupole model, for which $L = 500$ nm corresponds to 75 million atoms. For this size effect study, we calculate the Peierls stress in the twinning direction, where the shear strain ϵ_{xy} is applied on the $(11\bar{2})$ plane along the $-x[111]$ direction (see Fig. 3).

To study the twinning/anti-twinning asymmetry, we repeat calculations of the Peierls stress using the six model configurations. The twinning/anti-twinning directions in a cross section of the BCC lattice

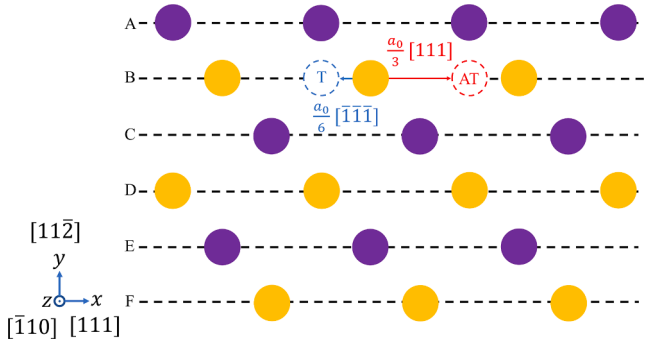

Fig. 3. Schematic of two opposite shearing directions on the {112} plane: twinning and anti-twinning directions. Atoms on different {110} planes are colored differently. T and AT denote twinning and anti-twinning directions, respectively.

are illustrated in Fig. 3. Along the twinning direction, the atoms only need to move by $(a_0/6)\langle 111\rangle$ on every $(11\bar{2})$ plane to form a twin. In contrast, the anti-twinning direction requires the atoms to move by $(a_0/3)\langle 111\rangle$ along the opposite direction to form a twin [67]. For these anti-twinning direction calculations, we fix the size $L = 50$ nm.

For all simulations described thus far, we apply the shear-controlled loading mode (Fig. 4(a)) that shears the entire cell with all atoms mapped to the deformed cell in strain increments of $\Delta\epsilon_{xy} = 10^{-5}$. This strain increment was proven sufficiently small to calculate the Peierls stress of an edge dislocation on the {110} plane in Fe [23]. Each time the strain increment is imposed, the total energy of the system is minimized using the conjugate gradient algorithm and followed by the fast inertial relaxation engine [68]. Minimization iterations are terminated when one of the following criteria is satisfied [69–71]: (1) the energy change between successive iterations divided by the energy magnitude is less than or equal to 10^{-12} or (2) the length of the global force vector for all atoms is less than or equal to 10^{-12} eV/Å. In the FBC and FBS models, atoms in the outer regions (marked in blue in Fig. 2) are fixed along the three directions during energy minimization. In the PAD model, atoms in the top and bottom regions are fixed along the x direction but are allowed to move along the other two directions. In the three remaining model configurations (dipole-H, dipole-V, and quadrupole), no atoms are constrained during the energy minimization. In every increment, the virial stress component, τ_{xy}, of the system is determined. When the edge dislocation moves from the original Peierls valley to the adjacent one, the corresponding value of τ_{xy} is the Peierls stress [23,25,29,31].

Last, we study the effects of loading mode, for which there are three: the shear-controlled loading mode described earlier, as well as the displacement-controlled [29] and stress-controlled [25,12,28] loading modes. The three loading modes are illustrated in Fig. 4. In the displacement-controlled loading mode, a displacement increment (corresponding to the strain increment $\Delta\epsilon_{xy} = 10^{-5}$) is applied to a layer of atoms (designated by the top red region), while those atomic layers within the bottom (red) region are fixed. Similar to the selection of the size for the blue regions in the FBC and FBS models in Fig. 2, the thickness of these red regions is slightly larger than the cutoff distance of the interatomic potential. Note that Cho et al. [72,73] and Dang and Spearot [74] constructed their displacement-controlled PAD models via a slightly different approach. In their models, atoms in the top and bottom regions are displaced by a gradient displacement field and the remaining atoms are displaced following the elasticity theory. As a result, the stress values measured each time the dislocation moves from one Peierls valley to the next one are invariant to the initial position. However, in the present PAD model, after the dislocation has completely moved to the next Peierls valley from the initial one, the stress achieved in subsequent translations may not be the same as that in the first one. Variance in the stress needed to move after the first Peierls stress is achieved also appeared in a previous work of Osetsky and Bacon [23], who used the same method. Thus, at least for the first translation, the PAD model should yield similar results as those used by Cho et al. [72,73], and Dang and Spearot [74]. This hypothesis will be confirmed in subsections 3.4.

In the stress-controlled loading mode, two opposite forces are exerted onto the atoms within the red regions near the top and bottom surfaces, giving rise to an applied stress component, τ_{xy}. The critical applied stress for the edge dislocation to start moving is found by the bisection method and the resultant error of Peierls stress is in ±0.5 MPa. For this study, the PAD model with $L = 50$ nm is utilized to calculate the Peierls stresses in both the twinning and anti-twinning directions. All other simulation settings are the same among three loading modes. As before, the strain increment and the applied stress are negative if the shear is directed along the twinning direction and are positive for the anti-twinning direction.

For verification, before embarking in these series of studies, we attempt to check the results against those published in the literature. For

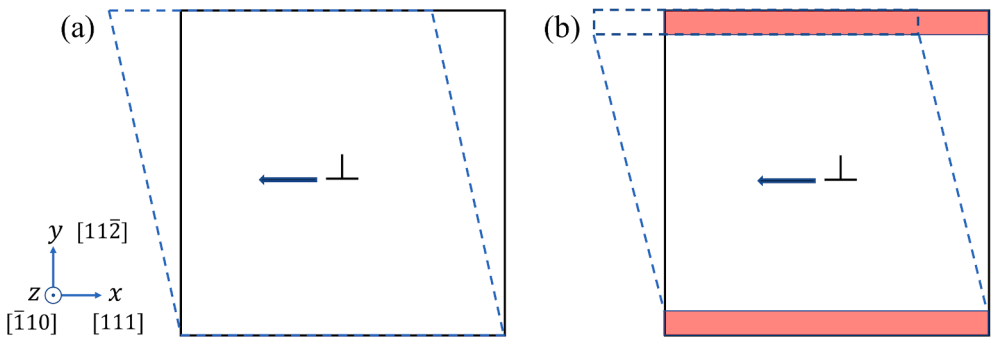

Fig. 4. Schematic of the MS simulation configurations with (a) shear-controlled and (b) stress- or displacement-controlled loading modes. In (b), the top and bottom regions are in red. In both subfigures, the loading direction is along the twinning direction.

Nb, a prior MS calculation of the Peierls stress for a screw dislocation on the {112} plane can be found in Ref [27]. For comparison, we employ the same FBC model with $L = 120$ nm and the same interatomic potential to calculate the Peierls stress for the $(a_0/2)\langle 111\rangle$ screw dislocation on a $(11\bar{2})$ plane. Like Ref. [27], we also introduced the screw dislocation by anisotropic elasticity theory. In our calculation, the shear-controlled loading mode was utilized and we obtained 1264.3 MPa, which is reasonably close to the 1130 MPa reported in Ref. [27]. We suspect the differences arise from the loading mode used, which was not reported in their work.

3. Results and Discussion

Figure 5 shows typical stress-strain curves obtained from the six different models for a simulation cell dimension $L = 100$ nm. For both potentials, the initial stress τ_{xy} is near-zero in all model configurations except the dipole-H model, in which τ_{xy} is negative. The negative initial stress in the dipole-H model may be attributed to that the interaction energy between the primary dipole and all the image dipoles is only conditionally convergent to a finite value [75,24]. Regardless of the initial stress, all curves are linear up to a strain at which the stress first drops, then rises again linearly, and in some cases followed by more stress drops. These stress drops are associated with the motion of the dislocation. The Peierls stress is thus the peak stress before the first stress drop, when the dislocation just begins to move (as indicated by the downward arrows). Clearly, the Peierls stresses predicted by Ackland potential are generally much higher than those by Lin potential, in line with the difference in their GSFE curves (Fig. 1).

3.1. Model configuration and size

Figure 6(a) shows the variation in the Peierls stress of the Ackland potential versus model size L. For all model configurations, the Peierls stress is size-dependent when $L < 40$ nm. In this regime, the smaller sizes give artificially lower Peierls stresses. For greater L, only with the PAD model does the Peierls stress achieve a stable value of 500 MPa that is independent of L, when $L > 100$ nm. For the remaining five models, however, the Peierls stress does not strictly converge as L increases, and its value continues to rise, albeit at a very small rate, even for $L = 500$ nm. Although the Peierls stresses do not saturate strictly after $L > 200$ nm, their increments with size could be viewed, to some extent, as tolerable. Regarding the magnitude, provided the model size $L > 100$ nm, the PAD configuration provides the lowest. By contrast, the remaining models obtain higher Peierls stresses that are $\sim$ 580 MPa at $L = 500$ nm.

Figure 6(b) presents the same size effect analysis on the Peierls stress of the Lin potential. As can be expected, when L is too small, where too small is $L < 40$ nm, the calculated values are size-dependent. For greater L, two model configurations, the PAD model ($L > 40$ nm) and FBC ($L > 300$ nm) model, provide converged Peierls stresses of 104 MPa and 177 MPa, respectively. In contrast, when employing the other model configurations, the computed Peierls stresses vary substantially as L increases. The variation behaves too irregularly, exhibiting substantial changes in stress of $\sim$ 20–100 MPa with increments in L of 100 nm. Even to the outstandingly large limit of $L = 500$ nm, the Peierls stress has not

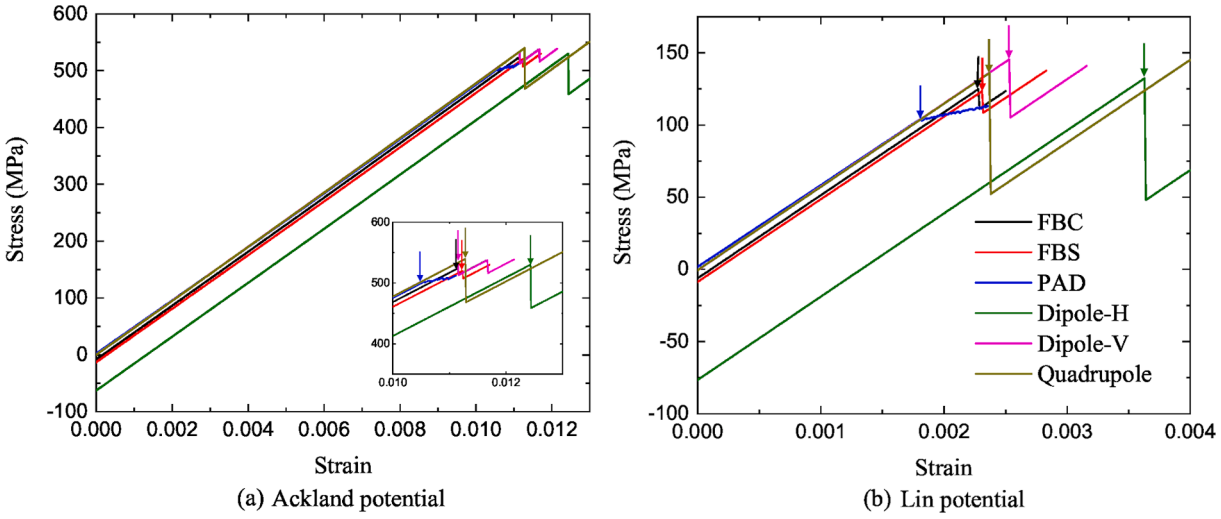

Fig. 5. Stress-strain curves in various models with cell dimension $L = 100$ nm by using (a) Ackland potential and (b) Lin potential. The solid arrows denote the Peierls stresses in the corresponding models.

converged. In terms of magnitude, they are all below 250 MPa, with the PAD model providing the lowest values. Clearly the model configuration has a substantial influence. Some configurations are unable to compute a Peierls stress that is independent of the model size even up to $L = 500$ nm.

Our simulations showed that, for the same model configuration, small simulation cells almost always predict lower Peierls stresses. The same size effect was recently reported in FCC Al using the dipole-H model and was attributed to the wider intrinsic stacking fault in smaller models [7]. Similarly, in the current work of Nb, smaller simulation cell sizes affect the dislocation core structure, resulting in lower Peierls stresses.

In FBS and FBC models, the fixed boundaries are constructed via the elasticity theory based on the initial position of the dislocation. As the dislocation moves, however, those boundaries are no longer compatible with the new dislocation-induced displacement field. Thus, the fixed boundaries exert a back stress on the dislocation, elevating the Peierls stress [76]. As shown in Fig. 6, the Peierls stresses predicted by the FBS/FBC models are among the highest.

Intuitively, dipole-H and quadrupole configurations should have lower Peierls stress due to the attractions between the neighboring, oppositely signed dislocations in the same cell. It should be noted there also exist attractive forces between the dislocations and their oppositely signed counterparts in adjacent periodic images. The latter attractive forces counter the former ones and hence prevent the Peierls stress from being low. Thus, the Peierls stresses for these two models are not the lowest in our simulations.

As the model size increases, only the PAD model configuration in our calculations displays the converged Peierls stress that also ranks the lowest among all model configurations. Compared with the FBS/FBC and the dipole/quadrupole models, the lower stress achieved in the PAD model may result from the absence of the back stress and fewer interactions between the dislocations and its periodic images, respectively.

The influence of model configuration has also been reported in a few studies. Pizzagalli and Beauchamp [77] compared the FBS and quadrupole models when calculating the Peierls stress of the screw dislocation on the shuffle-set glide plane in Si via DFT calculations and the shear-controlled loading mode. It was found that the calculated Peierls stress is $\sim 7\%$ higher in the FBS model than in the quadrupole model. There, the model sizes were smaller (128 and 144 atoms in the FBS and quadrupole models, respectively) due to the DFT method used and the model size dependence was not assessed. Segall et al [65] calculated the Peierls stress of a $a_0/2\{110\}\langle 111\rangle$ screw dislocation in BCC Ta via the shear-controlled loading model and a quantum-based, embedded atom force field developed by Strachan et al [78]. They achieved the convergence when the diameter of the FBC model is larger than 10 nm and pointed out that the Peierls stress of the quadrupole model approximates the converged value of FBC when L reaches about 8 nm. Considering the dimensions were also small (fewer than 6000 atoms), the similarity in the Peierls stresses between their quadrupole and FBC models may be a coincidence. From the results of the present study, we see each model configuration has an individual minimum size for convergence with Lin potential. When one or more of the Peierls stresses are not converged, the differences in value and even the rank order among the Peierls stresses calculated from different model configurations depend too strongly on the size to be meaningful. Convergence to the energy minimum state is dictated by an energy-based criterion rather than a force-based criterion. According to the former criterion, convergence is determined by the change in energy between successive iterations divided by the total energy in the system. Hence, the energy minimization procedure is to some extent size-dependent. However, this may not be the reason why the Peierls stresses are size-dependent because the PAD model predicts converged results, while using the same energy criterion.

For other dislocations in other materials, it is generally found that atomistic models overestimate the Peierls stress compared to experimental values [79] or those from DFT [18], owing to the quantum effect that cannot be captured by classical interatomic potentials [80]. Taking this view, it would appear that the lower the prediction the closer the calculated value is to the actual value, favoring the PAD model configurations. While it cannot be said that the value of the {112} Peierls stress is accurate against experimental measurement or DFT, at least for numerical exploration, a reasonable size atomic model can be defined with the PAD model configuration for which the Peierls stress computations would not be model size-dependent.

3.2. Twinning versus anti-twinning directions

The Peierls stress on the {112} plane depends on the sense of direction, commonly referred to as the twinning and anti-twinning directions [81–83]. As shown in Fig. 3, , atomic displacements in one sense require shorter displacements to form the twin structure, while in the opposite sense the displacements needed to achieve the same structure are larger. Further, the atomic layer, marked C, exerts more resistance to the anti-twinning shear than the twinning shear [67]. Here, we calculate the Peierls stresses using all six models with $L = 50$ nm for both the twinning and anti-twinning directions using the two EAM potentials and

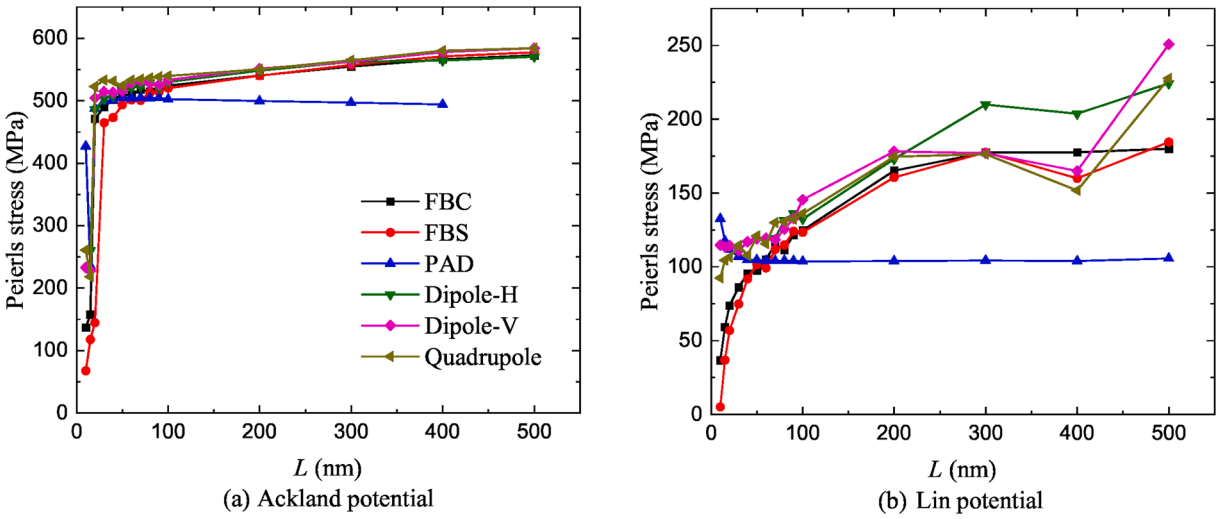

Fig. 6. Peierls stresses calculated in various model configurations as a function of cell dimension L by using (a) Ackland potential and (b) Lin potential.

the shear-controlled loading mode. It is recognized, however, that only the PAD model configuration yields converged Peierls stresses for this model size. Further, the dipole-H model configuration with the Lin potential is, however, not included, since the dislocation self annihilates during energy minimization when $L < 70$ nm, as mentioned in section 2.

Table 2 presents the Peierls stresses computed in the anti-twinning/twinning (AT/T) directions. For the material using the Ackland potential, the twinning Peierls stress is less than the anti-twinning Peierls stress, following expectation. This AT/T asymmetry is consistently predicted for all six model configurations. We find, however, that the model configuration affects the percentage difference between the two senses. The degree of asymmetry is the largest for the FBS model and approximately the same for the PAD, dipole-H, dipole-V, and quadrupole models. For the PAD model, the Peierls stresses have saturated for this model size. For the other model configurations, the Peierls stress in the Ackland material for sizes greater than $L = 50$ nm, very slowly and thus, the AT/T asymmetry and the degree of asymmetry, as measured by their differences, are not expected to change for larger L. The AT/T asymmetry is consistent with the conclusion in Refs. [84,85], where the critical stress to move the edge dislocation on a {112} plane in Fe in PAD model using the displacement-controlled loading mode was always lower along the twinning direction than the anti-twinning direction at 0, 1, 50, and 400 K. The same was observed in a recent work in Mo in PAD model using the shear-controlled loading mode in MS calculations at 0 K [86,87].

In the case of the Lin potential, the AT/T asymmetry depends on the model configuration used. For the FBC and FBS model, the Peierls stress along the twinning direction is lower than that along the anti-twinning direction. But for the remaining configurations, the anti-twinning value is oddly less than the twinning one. For the PAD prediction, this anomalous asymmetry is not expected to change for larger L since the stresses have converged for the size $L = 50$ nm used. Since the other potential considered predicts the anticipated AT/T asymmetry for the same model configurations, we suspect that the reverse asymmetry is a consequence of the Lin potential.

3.3. Isotropic or anisotropic elasticity theory

For the FBC and FBS models, a choice is made here to employ anisotropic elasticity theory, rather than isotropic elasticity theory, when first inserting the edge dislocation into the perfect lattice. In principle, the structure of the dislocation after relaxation and response of the dislocation under subsequent deformation ought not to be sensitive to the process in which the dislocation is first inserted, since the system is not yet stabilized. With this in mind, one may find it easier then to first insert the dislocation using isotropic elastic theory than the anisotropic one. Yet, as mentioned, in these two fixed boundary condition models, the boundaries are not minimized during relaxation and hence, the choice of elasticity theory for defining the dislocation displacements could matter.

It is worth emphasizing that this choice in the model design pertains to the method for inserting the dislocation prior to deformation, and is separate from the elastic anisotropy inherent to the interatomic potential. For Nb, the degree of elastic anisotropy is significant with a Zener ratio of $A_c = 2C_{44}/(C_{11} - C_{12}) = 0.5$, when using experimental values (Table 1). As mentioned, both the Ackland and Lin potentials predict similar values for the three elastic constants, and hence A_c, for Nb.

Figure 7 shows the change in the Peierls stress with system size L for the full range of sizes. In all simulations, the Peierls stress is calculated using the shear-controlled loading mode. Provided that $L > 100$ nm, for the Ackland potential, the type of elasticity theory used for dislocation insertion has little to no effect on the calculated Peierls stress. This size range, $L > 100$ nm, is the same size regime in which the Peierls stress is less sensitive to L. Yet, it may be undesirable that a relatively large simulation size (i.e., 574191 and 757080 atoms in FBC and FBS models, respectively) is required to remove any assumptions made in the dislocation introduction process.

For the Lin potential, the effect of the elasticity theory results in large fluctuations for both model configurations. For FBC wherein the Peierls stresses were seen to converge for $L > 300$ nm in the anisotropic case, they do not converge for the isotropic case even up to very large model sizes $L = 500$ nm. The difference grows rather than shrinks with size. In summary, even in situations where the fixed model configuration and potential combination produces a size-independent Peierls stress, it is still best to use anisotropic theory for introducing the dislocation.

3.4. Loading mode

By definition, the Peierls stress should be independent of the loading mode. Yet, part of the model design is choosing the method in which the system is incrementally mechanically deformed in order to drive the dislocation to first move. The displacement-controlled and the shear-controlled loading mode effectively exert a strain increment to region around the dislocation core. The stress-controlled loading mode, however, applied the stress directly. All three methods have been employed in the literature and it is expected that all three modes will compute similar Peierls stresses when all else is the same. To identify any possible influences of loading mode, as a component of model design, these three modes are used to calculate the Peierls stress in the T and AT directions. For this test, the PAD model configuration and $L = 50$ nm are employed, for which both interatomic potentials produce converged Peierls stresses in the shear loading mode. Table 3 compares the Peierls stresses resulting from the three different loading modes.

The Peierls stresses for the Lin potential are similar for all three modes, lying within 10% of each other, a result that follows expectation. For the Ackland potential, however, the Peierls stresses based on the stress-controlled loading mode are lower than those based on the shear- and displacement-controlled loading modes, with the latter two being similar. In addition, using the displacement-controlled PAD model designed by Cho et al [72] and Dang and Spearot [74], we calculate the Peierls stresses for the twinning and anti-twinning directions as 500.1 MPa and 527.7 MPa, respectively, using the Ackland potential. These values are close to the Peierls stress values based from the displacement-controlled PAD model, as shown in Table 3.

4. Conclusions

In this work, we aim to identify the importance of model design in

Table 2
Calculated Peierls stresses (in MPa) for the twinning and anti-twinning directions from various models with $L = 50$ nm and two different interatomic potentials. The superscripts T and AT represent twinning and anti-twinning directions, respectively. All the simulations here utilize the shear-controlled loading mode. Results are missing for the dipole-H model when using Lin potential, since the dislocation self annihilates during the energy minimization before loading when $L < 70$ nm, as mentioned in section 2. The relative differences in the Peierls stresses based on different models with respect to PAD model are provided in parentheses.

	FBC	FBS	PAD	Dipole-H	Dipole-V	Quadrupole
Ackland^{T}	509.2 (1.0%)	493.3 (−2.2%)	504.3	516.8 (2.5%)	515.8 (2.3%)	523.9 (3.9%)
Ackland^{AT}	577.3 (5.2%)	574.1 (4.6%)	548.9	567.1 (3.3%)	567.4 (3.4%)	565.6 (3.0%)
Lin^{T}	97.4 (−7.0%)	101.6 (−3.0%)	104.7		119.1 (13.8%)	120.9 (15.5%)
Lin^{AT}	120.6 (28.4%)	128.7 (37.1%)	93.9		99.0 (5.4%)	100.5 (7.0%)

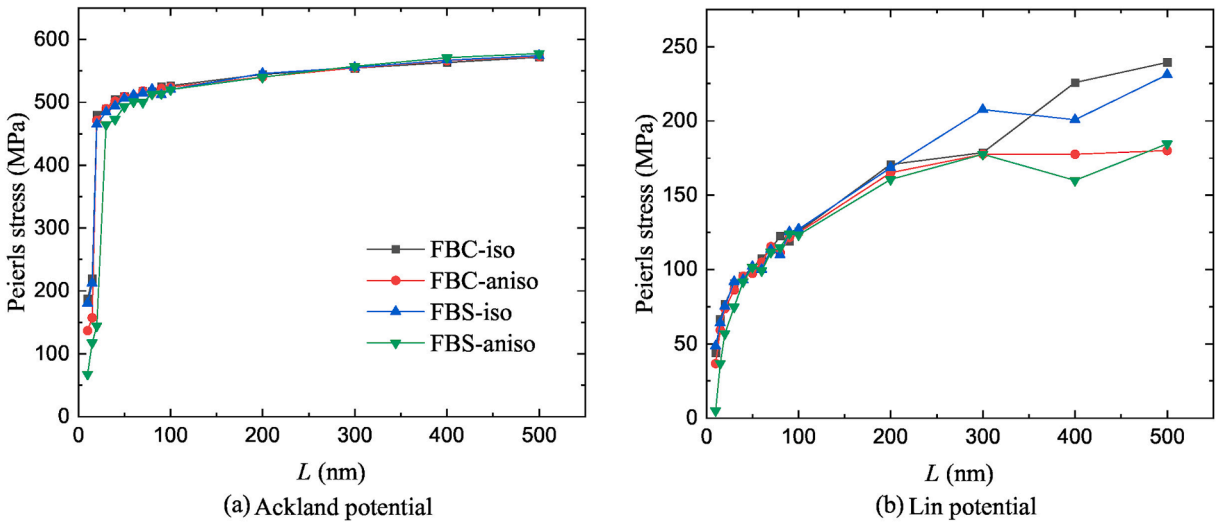

Fig. 7. Peierls stress calculated in FBC and FBS models with the dislocation introduced via isotropic (iso) or anisotropic (aniso) elasticity theory as a function of cell dimension L by using (a) Ackland potential and (b) Lin potential.

Table 3
A comparison in the Peierls stress (in MPa) using the PAD model with $L = 50$ nm, but with different interatomic potentials, loading modes, and shear directions. The superscripts T and AT represent twinning and anti-twinning directions, respectively.

	Shear-controlled	Displacement-controlled	Stress-controlled
Ackland^{T}	504.3	512.3	284.0
Ackland^{AT}	548.9	549.8	451.0
Lin^{T}	104.7	108.1	111.0
Lin^{AT}	93.9	95.6	99.0

molecular statics calculations of Peierls stresses in Nb. For the study, we employ two different interatomic potentials, the Ackland and Lin potential, since they provide similar lattice and elastic constants but greatly differing Peierls stress values. Interatomic potentials are continually being improved and the goal here is not to test the potentials but to identify a model design that produces consistent results and sensitivities among different potentials. Important settings involved in model design considered here are model configuration, for which there are six; model size, up to a relative large value of $L = 500$ nm; and loading mode. In order to comprehensively consider the wide range of settings used in the literature to date, we focus on the motion of the edge dislocation on the {112} plane, which possesses a natural twinning/anti-twinning asymmetry in glide. The study reveals that model design, as a whole, has a substantial effect on the computed values of the Peierls stress. Main conclusions are:

- Only one model configuration, the PAD model, achieves a strictly converged value for the two interatomic potentials considered here. The Peierls stress from most other model configurations continue to increase as size increases even up to $L = 500$ nm. In most cases, model sizes that are smaller than that required to reach a converged value predict artificially lower Peierls stresses.
- Two model configurations, the FBC and FBS models, utilize elasticity theory to introduce the dislocation into the perfect lattice. It is shown that the converged Peierls stress when using anisotropic theory-based dislocation insertion may become unconverged when using the isotropic theory instead.
- With the same interatomic potential, while one model configuration can predict a twinning Peierls stress lower than the anti-twinning Peierls stress, another model configuration can predict the opposite asymmetry.
- The shear-controlled and displacement-controlled loading modes are found to provide similar results as well as consistent results given the two potentials. The related LAMMPS input files for calculating the Peierls stress using different loading modes can be downloaded from https://github.com/wrj2018/CMS_2020.

While focusing on the edge dislocation on one slip plane, {112}, in one BCC metal, Nb, these results may be applicable to the edge dislocations on other slip planes, e.g., {110} and {123}, in Nb, and edge dislocations in other BCC metals as well as FCC and HCP metals. The findings here are anticipated to benefit the design of atomic models, such that they minimize the effects of simulation settings in the calculations of Peierls stresses.

5. Data availability

The raw/processed data required to reproduce these findings cannot be shared at this time as the data also forms part of an ongoing study.

Declaration of Competing Interest

The authors declare that they have no known competing financial interests or personal relationships that could have appeared to influence the work reported in this paper.

Acknowledgments

We thank Dr. Khanh Dang and Prof. Douglas Spearot for helpful discussions. W.J. and I.J.B. acknowledge funding in part from the Office of Naval Research under Grant No. N000141712810. S.X. acknowledges support in part from the Office of Naval Research under contract ONR BRC Grant N00014-18-1-2392. Use was made of computational facilities purchased with funds from the National Science Foundation (CNS-1725797) and administered by the Center for Scientific Computing (CSC). The CSC is supported by the CNSI and the Materials Research Science and Engineering Center (MRSEC; NSF DMR 1720256) at UC Santa Barbara.

References

[1] P.M. Anderson, J.P. Hirth, J. Lothe, Theory of Dislocations, Cambridge University Press, 2017.
[2] R. Peierls, The size of a dislocation, Proc. Phys. Soc. 52 (1) (1940) 34.

[3] F.R.N. Nabarro, Dislocations in a simple cubic lattice, Proc. Phys. Soc. 59 (2) (1947) 256.
[4] D.J. Bacon, Y.N. Osetsky, D. Rodney, in: L. Kubin, J.P. Hirth (Eds.), Dislocations in Solids, 15, Elsevier, 2009, pp. 1–90.
[5] D. Rodney, L. Ventelon, E. Clouet, L. Pizzagalli, F. Willaime, Ab initio modeling of dislocation core properties in metals and semiconductors, Acta Mater. 124 (2017) 633–659.
[6] V.V. Bulatov, E. Kaxiras, Semidiscrete variational Peierls framework for dislocation core properties, Phys. Rev. Lett. 78 (22) (1997) 4221–4224.
[7] S. Xu, J.R. Mianroodi, A. Hunter, B. Svendsen, I.J. Beyerlein, Comparative modeling of the disregistry and Peierls stress for dissociated edge and screw dislocations in Al, Int. J. Plast. 129 (2020) 102689.
[8] G. Liu, X. Cheng, J. Wang, K. Chen, Y. Shen, Peierls stress in face-centered-cubic metals predicted from an improved semi-discrete variation Peierls-Nabarro model, Scr. Mater. 120 (2016) 94–97.
[9] G. Liu, X. Cheng, J. Wang, K. Chen, Y. Shen, Atomically informed nonlocal semi-discrete variational Peierls-Nabarro model for planar core dislocations, Sci. Rep 7 (2017) 43785.
[10] K. Edagawa, Y. Kamimura, A.M. Iskandarov, Y. Umeno, S. Takeuchi, Peierls stresses estimated by a discretized Peierls-Nabarro model for a variety of crystals, Materialia 5 (2019) 100218.
[11] M. Ponga, K. Bhattacharya, M. Ortiz, Large scale ab-initio simulations of dislocations, J. Comput. Phys. 407 (2020) 109249.
[12] N.S. Weingarten, Dislocation mobility and Peierls stress of c-type screw dislocations in GaN from molecular dynamics, Comput. Mater. Sci. 153 (2018) 409–416.
[13] I. Shin, E.A. Carter, Possible origin of the discrepancy in Peierls stresses of fcc metals: First-principles simulations of dislocation mobility in aluminum, Phys. Rev. B 88 (6) (2013), 064106.
[14] M. Iyer, B. Radhakrishnan, V. Gavini, Electronic-structure study of an edge dislocation in aluminum and the role of macroscopic deformations on its energetics, J. Mech. Phys. Solids 76 (2015) 260–275.
[15] S. Das, V. Gavini, Electronic structure study of screw dislocation core energetics in Aluminum and core energetics informed forces in a dislocation aggregate, J. Mech. Phys. Solids 104 (2017) 115–143.
[16] A.M.Z. Tan, C. Woodward, D.R. Trinkle, Dislocation core structures in Ni-based superalloys computed using a density functional theory based flexible boundary condition approach, Phys. Rev. Mater. 3 (3) (2019), 033609.
[17] Y. Su, S. Xu, I.J. Beyerlein, Density functional theory calculations of generalized stacking fault energy surfaces for eight face-centered cubic transition metals, J. Appl. Phys. 126 (10) (2019) 105112.
[18] C.R. Weinberger, G.J. Tucker, S.M. Foiles, Peierls potential of screw dislocations in bcc transition metals: Predictions from density functional theory, Phys. Rev. B 87 (5) (2013), 054114.
[19] L. Dezerald, L. Ventelon, E. Clouet, C. Denoual, D. Rodney, F. Willaime, Ab initio modeling of the two-dimensional energy landscape of screw dislocations in bcc transition metals, Phys. Rev. B 89 (2) (2014), 024104.
[20] L. Romaner, C. Ambrosch-Draxl, R. Pippan, Effect of rhenium on the dislocation core structure in tungsten, Phys. Rev. Lett. 104 (19) (2010), 195503.
[21] M. Itakura, H. Kaburaki, M. Yamaguchi, First-principles study on the mobility of screw dislocations in bcc iron, Acta Mater. 60 (9) (2012) 3698–3710.
[22] M. Ghazisaeidi, L.G. Hector Jr., W. Curtin, First-principles core structures of ⟨c+a⟩ edge and screw dislocations in Mg, Scr. Mater. 75 (2014) 42–45.
[23] Y.N. Osetsky, D.J. Bacon, An atomic-level model for studying the dynamics of edge dislocations in metals, Modelling Simul. Mater. Sci. Eng. 11 (4) (2003) 427.
[24] W. Cai, V.V. Bulatob, J. Chang, J. Li, S. Yip, Periodic image effects in dislocation modelling, Phil. Mag. 83 (5) (2003) 539–567.
[25] J. Chaussidon, M. Fivel, D. Rodney, The glide of screw dislocations in bcc Fe: atomistic static and dynamic simulations, Acta Mater. 54 (13) (2006) 3407–3416.
[26] R. Gröger, A. Bailey, V. Vitek, Multiscalemodelingofplasticdeformationofmolybdenum and tungsten: I. Atomistic studies of the core structure and glide of 1/2 ⟨111⟩ screw dislocations at 0 K, Acta Mater. 56 (2008) 5401–5411.
[27] M.R. Fellinger, H. Park, J.W. Wilkins, Force-matched embedded-atom method potential for niobium, Phys. Rev. B 81 (14) (2010), 144119.
[28] A. Koester, A. Ma, A. Hartmaier, Atomistically informed crystal plasticity model for body-centered cubic iron, Acta Mater. 60 (9) (2012) 3894–3901.
[29] H. Lim, L. Hale, J. Zimmerman, C. Battaile, C. Weinberger, A multi-scale model of dislocation plasticity in α-Fe: Incorporating temperature, strain rate and non-Schmid effects, Int. J. Plast. 73 (2015) 100–118.
[30] S. Narayanan, D.L. McDowell, T. Zhu, Crystal plasticity model for BCC iron atomistically informed by kinetics of correlated kinkpair nucleation on screw dislocation, J. Mech. Phys. Solids 65 (2014) 54–68.
[31] L.M. Hale, J.A. Zimmerman, C.R. Weinberger, Simulations of bcc tantalum screw dislocations: Why classical inter-atomic potentials predict {112} slip, Comput. Mater. Sci. 90 (2014) 106–115.
[32] Cai W., Li J., Yip S., Molecular Dynamics, chap. 1, Elsevier, Amsterdam, 2012, 249–265.
[33] F.H. Stillinger, T.A. Weber, Computer simulation of local order in condensed phases of silicon, Phys. Rev. B 31 (8) (1985) 5262.
[34] Q. Ren, B. Joos, M. Duesbery, Test of the Peierls-Nabarro model for dislocations in silicon, Phys. Rev. B 52 (18) (1995) 13223.
[35] H. Koizumi, Y. Kamimura, T. Suzuki, Core structure of a screw dislocation in a diamond-like structure, Phil. Mag. A 80 (3) (2000) 609–620.
[36] S. Boffi, G. Caglioti, G. Rizzi, F. Rossitto, Glide systems and Peierls stresses in fcc and bcc metals from phonon energies, J. Appl. Phys. 44 (2) (1973) 603–607.
[37] M.S. Duesbery, Z.S. Basinski, On non-glide stresses and their influence on the screw dislocation core in body-centred cubic metals I. The Peierls stress, Proc. R. Soc. Lond. A 392 (1802) (1984) 145–173.
[38] S. Xu, Y. Su, D. Chen, L. Li, An atomistic study of the deformation behavior of tungsten nanowires, Appl. Phys. A 123 (12) (2017) 788.
[39] A. Seeger, U. Holzwarth, Slip planes and kink properties of screw dislocations in high-purity niobium, Phil. Mag. 86 (25–26) (2006) 3861–3892.
[40] R. Watanabe, Possible slip systems in body centered cubic iron, Mater. Trans. 47 (8) (2006) 1886–1889.
[41] C.R. Weinberger, B.L. Boyce, C.C. Battaile, Slip planes in bcc transition metals, Int. Mater. Rev. 58 (5) (2013) 296–314.
[42] J.W. Christian, S. Mahajan, Deformation twinning, Prog. Mater. Sci. 39 (1–2) (1995) 1–157.
[43] K. Kang, V.V. Bulatov, W. Cai, Singular orientations and faceted motion of dislocations in body-centered cubic crystals, Proc. Natl. Acad. Sci. USA 109 (38) (2012) 15174–15178.
[44] S. Xu, S.Z. Chavoshi, Uniaxial deformation of nanotwinned nanotubes in body-centered cubic tungsten, Curr. Appl. Phys. 18 (1) (2018) 114–121.
[45] T. Trusty, S. Xu, I.J. Beyerlein, Atomistic simulations of tungsten nanotubes under uniform tensile loading, J. Appl. Phys. 126 (9) (2019), 095105.
[46] R. Begley, J. Bechtold, Effect of alloying on the mechanical properties of niobium, J. Less Common Met. 3 (1) (1961) 1–12.
[47] S. Xu, Y. Su, L.T.W. Smith, I.J. Beyerlein, Frank-Read source operation in six body-centered cubic refractory metals, J. Mech. Phys. Solids 141 (2020) 104017.
[48] H. Warlimont, W. Martienssen (Eds.), Springer Handbook of Materials Data, 2 ed., Springer Handbooks, Springer International Publishing, 2018.
[49] S. Plimpton, Fast parallel algorithms for short-range molecular dynamics, J. Comp. Phys. 117 (1) (1995) 1–19.
[50] G. Ackland, R. Thetford, An improved *N*-body semi-empirical model for body-centred cubic transition metals, Phil. Mag. A 56 (1987) 15–30.
[51] D.-Y. Lin, S. Wang, D. Peng, M. Li, X. Hui, An n-body potential for a Zr-Nb system based on the embedded-atom method, J. Phys.: Condens. Matter 25 (10) (2013) 105404.
[52] Y. Su, S. Xu, I.J. Beyerlein, Ab initio-informed phase-field modeling of dislocation core structures in equal-molar CoNiRu multi-principal element alloys, Modelling Simul. Mater. Sci. Eng. 27 (8) (2019), 084001.
[53] S. Xu, J.K. Startt, T.G. Payne, C.S. Deo, D.L. McDowell, Size-dependent plastic deformation of twinned nanopillars in body-centered cubic tungsten, J. Appl. Phys. 121 (17) (2017) 175101.
[54] S. Xu, E. Hwang, W.-R. Jian, Y. Su, I.J. Beyerlein, Atomistic calculations of the generalized stacking fault energies in two refractory multi-principal element alloys, Intermetallics 124 (2020), 106844.
[55] S.M. Hafez Haghighat, J. von Pezold, C.P. Race, F. Körmann, M. Friák, J. Neugebauer, D. Raabe, Influence of the dislocation core on the glide of the $\frac{1}{2}\langle 111\rangle\{110\}$ edge dislocation in bcc-iron: An embedded atom method study, Comput. Mater. Sci. 87 (2014) 274–282.
[56] K.-I. Masuda, A. Sato, Electronic theory for screw dislocation in bcc transition metals, Philos. Mag. B 37 (4) (1978) 531–536.
[57] B. Douat, C. Coupeau, J. Bonneville, M. Drouet, L. Vernisse, L. Kubin, Atomic-scale insight into non-crystallographic slip traces in body-centred cubic crystals, Scr. Mater. 162 (2019) 292–295.
[58] B. Douat, J. Bonneville, M. Drouet, L. Vernisse, C. Coupeau, Low temperature atomic-scale observations of slip traces in niobium, Scr. Mater. 183 (2020) 81–85.
[59] H. Lim, J.D. Carroll, J.R. Michael, C.C. Battaile, S.R. Chen, J.M.D. Lane, Investigating active slip planes in tantalum under compressive load: Crystal plasticity and slip trace analyses of single crystals, Acta Mater. 185 (2020) 1–12.
[60] D. Chen, L.L. Costello, C.B. Geller, T. Zhu, D.L. McDowell, Atomistic modeling of dislocation cross-slip in nickel using free-end nudged elastic band method, Acta Mater 168 (2019) 436–447.
[61] X.-G. Li, C. Chen, H. Zheng, Y. Zuo, S.P. Ong, Complex strengthening mechanisms in the NbMoTaW multi-principal element alloy, npj Comput, Mater 6 (2020) 70.
[62] W.-R. Jian, M. Zhang, S. Xu, I.J. Beyerlein, Atomistic simulations of dynamics of an edge dislocation and its interaction with a void in copper: a comparative study, Modelling Simul. Mater. Sci. Eng. 28 (4) (2020), 045004.
[63] J. Hirth, J. Lothe, Theory of Dislocations, Wiley, New York, 1982.
[64] V.V. Bulatov, O. Richmond, M.V. Glazov, An atomistic dislocation mechanism of pressure-dependent plastic flow in aluminum, Acta Mater 47 (12) (1999) 3507–3514.
[65] D. Segall, T. Arias, A. Strachan, W. Goddard, Accurate calculations of the Peierls stress in small periodic cells, J. Comput.-Aided Mater. Des. 8 (2–3) (2001) 161–172.
[66] S. Xu, L. Xiong, Y. Chen, D.L. McDowell, An analysis of key characteristics of the Frank-Read source process in FCC metals, J. Mech. Phys. Solids 96 (2016) 460–476.
[67] J. Wang, Z. Zeng, M. Wen, Q. Wang, D. Chen, Y. Zhang, P. Wang, H. Wang, Z. Zhang, S.X. Mao, et al., Anti-twinning in nanoscale tungsten, Sci. Adv. 6 (23) (2020) eaay2792.
[68] E. Bitzek, P. Koskinen, F. Gähler, M. Moseler, P. Gumbsch, Structural relaxation made simple, Phys. Rev. Lett. 97 (17) (2006), 170201.
[69] S. Xu, J.R. Mianroodi, A. Hunter, I.J. Beyerlein, B. Svendsen, Phase-field-based calculations of the disregistry fields of static extended dislocations in FCC metals, Phil. Mag. 99 (11) (2019) 1400–1428.
[70] S. Xu, L. Smith, J.R. Mianroodi, A. Hunter, B. Svendsen, I.J. Beyerlein, A comparison of different continuum approaches in modeling mixed-type dislocations in Al, Modelling Simul. Mater. Sci. Eng. 27 (7) (2019), 074004.

[71] S. Xu, Y. Su, I.J. Beyerlein, Modeling dislocations with arbitrary character angle in face-centered cubic transition metals using the phase-field dislocation dynamics method with full anisotropic elasticity, Mech. Mater. 139 (2019) 103200.
[72] J. Cho, T. Junge, J.-F. Molinari, G. Anciaux, Toward a 3D coupled atomistic and discrete dislocation dynamics simulation: dislocation core structures and Peierls stresses with several character angles in FCC aluminum, Adv. Model. Simul. Eng. Sci. 2 (1) (2015) 1–17.
[73] J. Cho, J.-F. Molinari, G. Anciaux, Mobility law of dislocations with several character angles and temperatures in FCC aluminum, Int. J. Plast. 90 (2017) 66–75.
[74] K. Dang, D. Spearot, Pressure dependence of the Peierls stress in aluminum, JOM 70 (7) (2018) 1094–1099.
[75] W. Cai, V.V. Bulatov, J. Chang, J. Li, S. Yip, Anisotropic elastic interactions of a periodic dislocation array, Phys. Rev. Lett. 86 (25) (2001) 5727–5730.
[76] E. Clouet, Ab Initio Models of Dislocations, Handbook of Materials Modeling: Methods: Theory and Modeling (2020) 1503–1524.
[77] L. Pizzagalli, P. Beauchamp, First principles determination of the Peierls stress of the shuffle screw dislocation in silicon, Phil. Mag. Lett. 84 (11) (2004) 729–736.
[78] A. Strachan, T. Çağin, O. Gülseren, S. Mukherjee, R.E. Cohen, W.A. GoddardIII, First principles force field for metallic tantalum, Modelling Simul. Mater. Sci. Eng. 12 (4) (2004) S445.
[79] Y. Kamimura, K. Edagawa, S. Takeuchi, Experimental evaluation of the Peierls stresses in a variety of crystals and their relation to the crystal structure, Acta Mater 61 (1) (2013) 294–309.
[80] L. Proville, D. Rodney, M.-C. Marinica, Quantum effect on thermally activated glide of dislocations, Nature Mater 11 (10) (2012) 845–849.
[81] M. Yamaguchi, V. Vitek, Core structures of non screw $\frac{1}{2}\langle 111\rangle$ dislocations on {112} planes in bcc crystals. II. Peierls stresses and the effects of an external shear stress on the cores, J. Phys. F: Met. Phys. 5 (1) (1975) 11–16.
[82] M.S. Duesbery, V. Vitek, Plastic anisotropy in bcc transition metals, Acta Mater 46 (5) (1998) 1481–1492.
[83] K. Ito, V. Vitek, Atomistic study of non-Schmid effects in the plastic yielding of bcc metals, Philos. Mag. A 81 (5) (2001) 1387–1407.
[84] G. Monnet, D. Terentyev, Structure and mobility of the $\frac{1}{2}\langle 111\rangle\{112\}$ edge dislocation in BCC iron studied by molecular dynamics, Acta Mater. 57 (2009) 1416–1426.
[85] S. Queyreau, J. Marian, M. Gilbert, B. Wirth, Edge dislocation mobilities in bcc Fe obtained by molecular dynamics, Phys. Rev. B 84 (6) (2011), 064106.
[86] F. Wang, G.H. Balbus, S. Xu, Y. Su, J. Shin, P.F. Rottmann, K.E. Knipling, J.-C. Stinville, L.H. Mills, O.N. Senkov, I.J. Beyerlein, T.M. Pollock, D.S. Gianola, Multiplicity of dislocation pathways in a refractory multiprincipal element alloy, Science 370 (6512) (2020) 95–101.
[87] S. Xu, Y. Su, W.-R. Jian, I.J. Beyerlein, Local slip resistances in equal-molar MoNbTi multi-principal element alloy, Acta. Mater. 202 (2021) 68–79.